CHEMISTRY OF MATERIALS
Cite This: Chem. Mater. 2019, 31, 3974−3983
Article
pubs.acs.org/cm

High-Efficiency Violet-Emitting All-Inorganic Perovskite Nanocrystals Enabled by Alkaline-Earth Metal Passivation

Jia-Kai Chen,[†,¶] Ju-Ping Ma,[†,¶] Shao-Qiang Guo,[‡,¶] Ya-Meng Chen,[†] Qing Zhao,[§] Bin-Bin Zhang,[†] Zhi-Yong Li,[†] Yang Zhou,[†] Jingshan Hou,[∥] Yoshihiro Kuroiwa,[§] Chikako Moriyoshi,[§] Osman M. Bakr,[⊥] Junying Zhang,[*,‡] and Hong-Tao Sun[*,†,#]

[†]College of Chemistry, Chemical Engineering and Materials Science, Soochow University, Suzhou, Jiangsu 215123, China
[‡]Department of Physics, Beihang University, Beijing 100191, China
[§]Department of Physical Science, Hiroshima University, Higashihiroshima, Hiroshima 739-8526, Japan
[∥]School of Materials Science and Engineering, Shanghai Institute of Technology, Shanghai 201418, China
[⊥]Division of Physical Sciences and Engineering, King Abdullah University of Science and Technology (KAUST), Thuwal 23955-6900, Saudi Arabia
[#]State Key Laboratory of Luminescence and Applications, Changchun Institute of Optics, Fine Mechanics and Physics, Chinese Academy of Sciences, Changchun 130033, China

Supporting Information

ABSTRACT: Cesium lead halide perovskite nanocrystals (NCs) have emerged as promising luminescent materials for a range of applications. However, the creation of highly luminescent violet-emitting $CsPbCl_3$ NCs mostly relies on doping of a limited number of small-sized metal ions or post-synthetic surface treatment of NCs. Alkaline-earth (AE) metals (e.g., Ca^{2+}, Sr^{2+}, and Ba^{2+}) have been proposed to be able to substitute Pb^{2+} in halide perovskites, yet it remains incompletely understood whether AE metal ions can be incorporated into the perovskite lattice or can be merely situated at the surface. Here, we explore the possibility of using AE metal ions for the suppression of the formation of trap centers, which leads us to develop a one-pot synthetic passivation strategy to boost the violet-emitting efficiency of $CsPbCl_3$ NCs through the creation of a Ca^{2+}/Sr^{2+} involved passivation layer. The photoluminescence quantum yield of violet emission reaches 77.1% by incorporating an optimal amount of Ca^{2+}. A wide range of optical and structural characterizations, coupled with first-principles calculations, aid in clarifying the underlying mechanism for the AE-metal-dependent passivation of $CsPbCl_3$ NCs. Specifically, based on the experimental and theoretical results, a model is proposed for the observed abnormal incorporation phenomenon of AE^{2+} ions in NCs (i.e., Ba^{2+} can be incorporated into the core of NCs, Ca^{2+}/Sr^{2+} can only be at/near the surface, while Mg^{2+} can neither be in the core nor at the surface). We believe that the knowledge gained here may not only offer a new perspective to obtain high-efficiency violet-emitting perovskite NCs through a one-pot synthetic passivation but can also help elucidate the functions that AE^{2+} ions play in the optimization of perovskite optoelectronic devices.

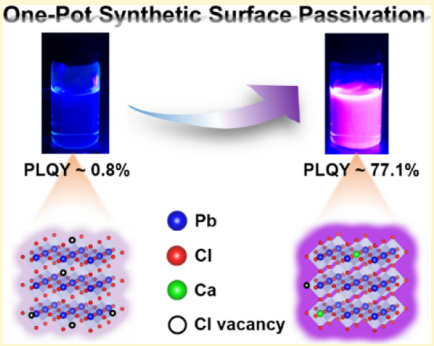

INTRODUCTION

Lead halide perovskites have aroused intense scientific attention owing to their low cost and outstanding optoelectronic properties, which lend them to applications in high-efficiency solar cells,[1−5] photo and radiation detectors,[6−8] and light-emitting devices.[9−12] So far, a diversity of organic-inorganic and all-inorganic halide perovskites have been developed for targeted applications. All-inorganic cesium lead halide perovskite ($CsPbX_3$, X = Cl, Br, I, or mixture of thereof) nanocrystals (NCs) show some arresting optoelectronic properties including tunable band gap, narrow emission line width, and high photoluminescence quantum yield (PLQY),[13−19] which make them be widely used as light emitters in a range of optoelectronic devices such as light-emitting diodes,[20−22] single-photon sources,[23−25] X-ray scintillators,[26] and lasers.[27,28] However, in contrast to $CsPbBr_3$ and $CsPbI_3$ NCs, $CsPbCl_3$ NCs show relatively low PLQY, which greatly hinders their potential applications.[16,21,29,30] The intrinsic mechanism for the low PLQY in $CsPbCl_3$ NCs lies in the low defect formation energy in the NC's core and/or at the surface. In our previous work, detailed theoretical calculations suggested that the defect formation energy of atomic vacancies like chlorine (Cl) vacancies in $CsPbCl_3$ NCs is low under Cl-poor synthetic conditions, leading to the occurrence of a large

Received: January 29, 2019
Revised: May 7, 2019
Published: May 8, 2019

DOI: 10.1021/acs.chemmater.9b00442
Chem. Mater. 2019, 31, 3974−3983

number of Cl vacancies. Such defects can bring about in-gap states, which act as nonradiative traps for the photogenerated charge carriers and thus result in low PLQYs.[31] We found that doping nickel ions into halide perovskite lattices could greatly increase the defect formation energies of the $CsPbCl_3$ lattice and gave rise to near-unity PLQY. Recent work by Samanta et al. showed that doping other small-sized cations such as Cd^{2+} could also increase the PLQY to near unity.[32] Similarly, doping of other kinds of metal cations can also boost the PLQY of the band-edge emission.[33−36] Another possible route for the attainment of highly luminescent $CsPbCl_3$ NCs is based on the post-synthetic surface treatment, which eliminates the trapping centers at or near the surface region.[37−40]

The alkaline-earth (AE) metals are a group of chemical elements in the s-block of the periodic table with very similar properties, all of which readily lose their two outermost electrons to form cations with a 2+ charge. Owing to comparable or relatively smaller ionic radii of AE^{2+} ions with respect to that of Pb^{2+} (e.g., the ionic radii of six-coordinate Sr^{2+}, Ca^{2+}, and Pb^{2+} are 1.18, 1, and 1.19 Å, respectively[41]), AE metals have been proposed to be able to substitute Pb in the perovskite structure in terms of the classical notion of Goldschmidt's rules and quantum mechanical principles. For instance, Navas et al. investigated the effect of Sr^{2+} or Ca^{2+} doping on the structure and photophysical properties of $CH_3NH_3PbI_3$ and proposed that the band gaps were decreased upon doping.[42] However, Sessolo et al. reported contrary behavior that the valence band maximum and Fermi level did not change with doping of Sr^{2+} in $CH_3NH_3PbI_3$ thin films.[43] Despite this inconsistence, previous results have reached a consensus that AE metal doping can decrease the defect concentration and result in improved performance of constructed devices.[44−48] We were thus intrigued whether doping of AE metal into $CsPbCl_3$ NCs can lead to suppression of structural defects, either in the NC's core or at the surface, and result in the high-efficient violet emissions. Importantly, using NC as an example system, we can survey the impact of AE metal introduction on the structure and photophysical properties of halide perovskites, considering that previous works mainly focused on perovskite films that possess multiple grain boundaries. The insights gained offer new perspectives to obtain high-efficiency violet-emitting perovskite NCs and potentially solve the controversies in the literature available, given that it remains incompletely understood whether AE metal ions are incorporated into the lattice or merely sit at the surface of halide perovskites.

Here, we provide a detailed examination of the influence of AE metal introduction on the structure and photophysical properties of $CsPbCl_3$ NCs based on a combination of experiments and theoretical calculations. All these NCs were synthesized by adding AE metal chloride into the reaction solution. We find that the photophysical properties are closely associated with the species and amount of AE metal introduced. Interestingly, the PLQY of violet-emitting $CsPbCl_3$ NCs can be boosted to 77.1% when incorporating an optimal amount of $CaCl_2$ in the synthesis, which is much higher than that synthesized without using any foreign cation. Detailed experimental analyses by X-ray photoelectron spectra and X-ray absorption spectra, combined with first-principles calculations, lead us to conclude that Ca^{2+} and Sr^{2+} ions are merely located at the surface of NCs, whereas Ba^{2+} ions are located at both the core and surface region. We propose that Ca^{2+} and Sr^{2+} ions form a passivation layer at the NC's surface, thus eliminating the trapping centers that are detrimental to radiative recombination of photogenerated charge carriers.

EXPERIMENTAL SECTION

Chemicals. Cesium carbonate (Cs_2CO_3, Aladdin, 99.99%), lead(II) chloride ($PbCl_2$, Alfa Aesar, 99.999%), magnesium chloride ($MgCl_2$, Aladdin, 99.99%), calcium chloride ($CaCl_2$, Macklin, 99.99%), strontium chloride hexahydrate ($SrCl_2{\cdot}6H_2O$, Aladdin, 99.99%), barium chloride dihydrate ($BaCl_2{\cdot}2H_2O$, Aladdin, 99.99%), oleic acid (OA, Alfa Aesar, 90%), oleylamine (OAm, Acros, approximate C18-content 80−90%), tri-*n*-octylphosphine (TOP, Alfa Aesar, 90%), 1-octadecene (ODE, Alfa Aesar, 90%), methyl acetate (MA, Alfa Aesar, 99%), *n*-hexane (Hex, GC, ≥98.0%), rhodamine B (Rhb, Aladdin, ≥AR), ethanol absolute (Aladdin, ≥99.8%), and pyridine (Macklin, 99.5%) were used without purification unless otherwise noted.

Preparation of Cs-Oleate Solution. Cs_2CO_3 (0.4073 g), ODE (15 mL), and OA (1.35 mL) were added to a 50 mL three-neck flask in the glovebox and dried for 1 h at 120 °C. Then, the mixtures were stirred under N_2 at 150 °C until all Cs_2CO_3 was dissolved.

Synthesis of $CsPbCl_3$ Perovskite NCs. $PbCl_2$ (0.0578 g), ODE (5 mL), OAm (0.8 mL), OA (0.8 mL), and TOP (1 mL) were added to a 50 mL three-neck flask in the glovebox and dried for 1 h at 120 °C. Then, the mixture was stirred under N_2 at 120 °C for 10 min. During stirring, dried OAm (0.8 mL) and dried OA (0.8 mL) were added slowly to the solution. After that, the temperature of the solution was raised to 210 °C, and this temperature was maintained for 5 min. Then, Cs-oleate (0.4 mL) was swiftly injected, and after 1 min, the solution was cooled in an ice bath.

Synthesis of AE^{2+}-$CsPbCl_3$ Perovskite NCs. $PbCl_2$ (0.0578 g), ODE (5 mL), OAm (0.8 mL), OA (0.8 mL), TOP (1 mL), and AE metal chloride (0.0396 g for $MgCl_2$; 0.0462 g for $CaCl_2$; 0.1109 g for $SrCl_2{\cdot}6H_2O$; 0.1016 g for $BaCl_2{\cdot}2H_2O$) were added to a 50 mL three-neck flask in the glovebox and dried for 1 h at 120 °C. After drying, the solution was stirred under N_2 at 120 °C for 10 min. At this time, dried OAm (0.8 mL) and dried OA (0.8 mL) were added slowly. Then, the solution was heated to 210 °C and maintained for 5 min. The as-prepared Cs-oleate (0.4 mL) was then swiftly injected, and after 1 min, the solution was cooled in an ice bath. The obtained samples were termed as AE^{2+}-$CsPbCl_3$ NCs.

Isolation and Purification of $CsPbCl_3$ Perovskite NCs. The crude solution was centrifuged at 12 000 rpm for 5 min, and the supernatant was discarded. This process was repeated twice. The precipitation was then dispersed in 2 mL of *n*-hexane and centrifuged at 12 000 rpm for 5 min, and the supernatant was discarded. Then, the precipitation was dispersed in 2 mL of *n*-hexane again and was centrifuged at 2000 rpm for 5 min. After that, the supernatant was extracted, followed by addition of 1 mL of MA in it. The mixed solution was centrifuged at 12 000 rpm for 5 min to precipitate perovskite NCs. The NC precipitation was then dispersed in 2 mL of *n*-hexane one more time and centrifuged at 12 000 rpm for 5 min. At last, the supernatant was extracted for the subsequent characterization.

NC Etching with Pyridine. The obtained AE^{2+}-$CsPbCl_3$ NCs solution was evaporated under vacuum at room temperature, and the precipitation was redispersed in 1 mL of pyridine. The NC-pyridine solution was stirred at 500 rpm for 2 h. After that, the resultant solution was centrifuged at 12 000 rpm for 5 min to precipitate perovskite NCs.

Optical Characterization. The absorption spectra were taken by a double-beam UV−vis−NIR spectrophotometer (Cary 5000, Agilent). The steady-state PL spectra were collected by a spectrometer equipped with a continuous (450 W) xenon lamp (FLS980, Edinburgh Instrument). Time-resolved PL measurements were reported on a Lifespec II setup (Edinburgh Instrument, UK) with the excitation of a picosecond-pulsed 373 nm laser (pulse width: 43 ps), and the excitation energy density is 4.0 $\mu J/cm^2$. To eliminate the reabsorbance effect of NCs, all NC solutions were diluted to an optical density of ca. 0.08. The PLQYs of all samples were calculated

DOI: 10.1021/acs.chemmater.9b00442
Chem. Mater. 2019, 31, 3974−3983

using Rhb as a reference sample, and the detailed calculations are shown in the Supporting Information (Figure S1).

Composition, XRD, XPS, and TEM Characterizations. The actual ion concentrations of lead and AE metal ions were taken by inductively coupled plasma-mass spectrometry (ICP-MS) (iCAPTM Qc, Thermo Scientific). The laboratory X-ray diffraction (XRD) spectra were taken using a Bruker D2 PHASER diffractometer with Cu Kα radiation (λ = 1.54056 Å). The high-resolution synchrotron XRD patterns were recorded on the BL02B2 beam line of SPring-8 at room temperature. The NC *n*-hexane solution was dried under vacuum at room temperature. The obtained precipitation was redispersed in 2 mL of mixed solvent (1 mL *n*-hexane and 1 mL MA), which was subsequently centrifuged at 12 000 rpm for 5 min to collect the precipitation. Then, the NCs were washed two more times according to the above procedure. The obtained dried powders were sealed into Hilgenberg glass capillaries with an inner diameter of 0.5 mm. The capillaries were rotated during the measurement to reduce the preferred orientation effect and to average the intensity. The X-ray wavelength used is 0.7997 Å. We found that the presence of a large number of organic ligands can affect the stability of NC powders. Thus, the samples for the synchrotron XRD were washed by MA three times to remove the excess organic ligands and to keep the phase stability after a long-term transportation before measurements, although this affects the dispersity. XPS data were obtained on a Rigaku XPS-7000 spectrometer. To prepare the samples for the XRD and XPS measurements, the NC solution was evaporated under vacuum at room temperature, and the precipitation was redispersed in toluene to form a concentrated NC solution. Then, the concentrated solution was drop-cast onto a glass substrate for the XRD measurement or a silicon substrate for the XPS measurement. TEM images were obtained by a FEI Tecnai G20 S-TWIN TMP microscope operating at an accelerating voltage of 200 kV.

X-ray Absorption Measurement. The X-ray absorption spectra of Pb L_{III}-edge for the Ca^{2+}-$CsPbCl_3$ NCs were obtained on the BL14W1 beam line at Shanghai Synchrotron Irradiation Facility. For the measurement, the sample was dispersed on a single-faced adhesive tape (Scotch). The Pb (Alfa Aesar, 99.9%) and $PbCl_2$ (Alfa Aesar, 99.999%) powders were used as reference samples. To remove the surface oxide layer, Pb powder was treated at 150 °C for 1 h in a reducing atmosphere (H_2/N_2: 5%). All X-ray absorption spectra were taken at room temperature, and the data were collected in the transmission mode. The obtained data were analyzed using the IFEFFIT software package.

First-Principles Calculations. The band structures and density of states (DOSs) of $CsPbCl_3$ with dual defects containing AE metal dopant and vacancy (V_{Cs}, V_{Cl}, and V_{Pb}) were simulated using the Vienna Ab initio package (VASP),[49] on the basis of noncollinear projector-augmented waves method.[50] We use Perdew–Burke–Ernzerhof version of generalized gradient approximation to describe the electron exchange–correlation potential.[51] The plane-wave basis cutoff energy is set at 450 eV. The Brillouin zone is sampled with the Monkhorst–Pack centered meshes of the *K* points with 3 × 3 × 3, the ions were relaxed until the maximum forces were less than 0.01 eV·Å^{-1}, and the total energy was converged to 1 × 10^{-4} eV/atom.

In band structures and DOSs, the zero energy point was set to the Fermi level of the pure $CsPbCl_3$. The system with the defects was corrected by aligning the average electrostatic potential (V_{av}) of Cs atoms located far from the defects to the V_{av} for the same elements in the pure $CsPbCl_3$.[52] To examine the feasibility of incorporating different defects into the lattice, the defect formation energy was calculated using the following formulas

$$E_{form}^{vac} = E_{total}(\text{X vac}) - [E_{total}(\text{pure}) - \mu_X] \quad (1)$$

$$E_{form}^{doped} = E_{total}(\text{AE doped}) - [E_{total}(\text{pure}) + \mu_{AE} - \mu_{Pb}] \quad (2)$$

$$E_{form}^{mixed} = E_{total}(\text{mixed}) - [E_{total}(\text{pure}) + \mu_{AE} - \mu_X - \mu_{Pb}] \quad (3)$$

where E_{form}^{vac}, E_{form}^{doped}, and E_{form}^{mixed} represent X vacancy formation energy, AE (Mg, Ca, Sr, and Ba) dopant formation energy, and dual defect (that contains AE dopant and vacancy) formation energy, respectively. X represents the chemical elements of Cs, Pb, or Cl. E_{total}(pure), E_{total}(X vac), E_{total}(AE doped), and E_{total}(mixed) are the total energies of 3 × 3 × 3 supercells for undoped, X vacancy, AE doped, and dual defects containing $CsPbCl_3$, respectively. μ_{Cs}, μ_{Pb}, and μ_{Cl} are the chemical potentials of Cs, Pb, and Cl atoms, respectively. The stability region of different compounds against Cl and Pb chemical potentials has been calculated as shown in ref 31. μ_{AE} is the chemical potentials of AE atom, which depends on the experimental synthetic environments of Cl-poor, Cl-rich, or anything in between. Under the Cl-poor condition, μ_{AE} is calculated from the bulk solid phase of AE. Chemical potentials of μ_{AE} and μ_{Cl} satisfy the following condition

$$2\mu_{Cl} + \mu_{AE} = \mu_{AECl_2} \quad (4)$$

where u_{Cl} is obtained from free molecule Cl_2.

RESULTS AND DISCUSSION

We synthesized AE^{2+}-$CsPbCl_3$ NCs by a modified hot-injection method as first reported by Protesescu et al.[16] The injection temperature was raised to 210 °C, and the reaction time was extended to 1 min. The AE chlorides were used as the sources of AE ions. For the synthesis of AE^{2+}-$CsPbCl_3$ NCs, we added a certain amount of AE metal chloride in the reaction system (see details in the Experimental Section). These AE^{2+}-$CsPbCl_3$ NCs were first examined by the laboratory XRD, which suggests the formation of the cubic perovskite structure (Figure S2). We note that, although there are no obvious shift of diffraction peaks for Mg^{2+}-, Sr^{2+}-, or Ca^{2+}-$CsPbCl_3$ NCs with respect to that of pristine ones, a slight shift to low angles for Ba^{2+}-$CsPbCl_3$ NCs can be observed. Owing to the low resolution of the laboratory XRD, we then took the high-resolution synchrotron XRD measurement. As shown in Figure 1a, compared with the pristine cousin, the diffraction peak at about 11.58° for Ba^{2+}-$CsPbCl_3$

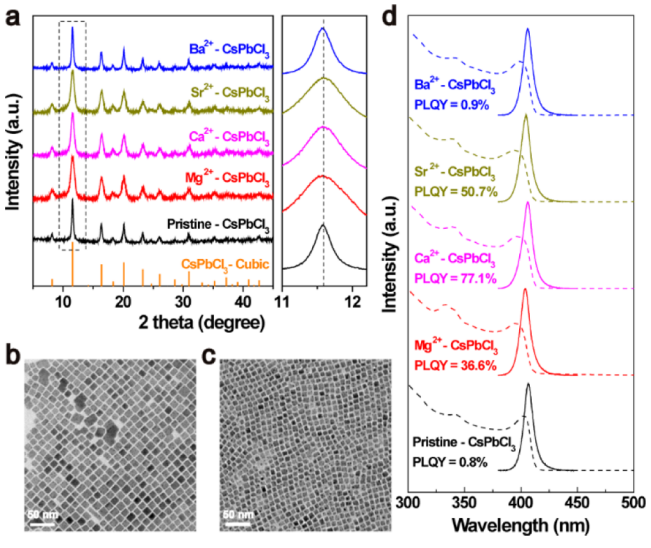

Figure 1. (a) High-resolution synchrotron XRD patterns of pristine and AE^{2+}-$CsPbCl_3$ NCs. An enlarged view of the peaks marked by the dotted outline is shown in the right panel, in which the dotted vertical line is drawn to guide the eye. (b,c) TEM images of pristine $CsPbCl_3$ NCs with an average edge length of ~12.6 nm (b) and Ca^{2+}-$CsPbCl_3$ NCs of ~8.4 nm, with a Ca^{2+}/Pb^{2+} ratio of 10.5% (c). (d) UV–vis absorption (dotted line) and PL (solid line) spectra of pristine and AE^{2+}-$CsPbCl_3$ NCs. The molar ratios of AE^{2+}/Pb^{2+} in Mg^{2+}, Ca^{2+}, Sr^{2+}, and Ba^{2+}-$CsPbCl_3$ NCs are 0, 10.5, 5.9, and 12.3%, respectively.

DOI: 10.1021/acs.chemmater.9b00442
Chem. Mater. 2019, 31, 3974–3983

NCs indeed has a slight low-angle shift. Transmission electron microscopy (TEM) images of these samples indicate the NCs have uniform cubic morphology with good monodispersity (Figures 1b,c and S3). Interestingly, introducing AE^{2+} ions decreases the average size of the NCs, from 12.6 nm of the pristine NCs to 8.4 nm of Ca^{2+}-$CsPbCl_3$, for example (Figures 1b,c and S4).

Figure 1d shows the absorption and luminescence spectra of as-prepared AE^{2+}-$CsPbCl_3$ NCs. All these NCs demonstrate PL with a small Stokes shift and a narrow full width at half-maximum of ca. 10 nm. Interestingly, we find that the PLQYs of these NCs are markedly different: pristine and Ba^{2+}-$CsPbCl_3$ NCs have extremely low PLQYs, whereas Mg^{2+}, Ca^{2+}, and Sr^{2+}-$CsPbCl_3$ NCs show greatly enhanced PLQYs. The PLQY of Ca^{2+}-$CsPbCl_3$ NCs can be as high as 77.1%. Time-resolved PL results show the lengthened lifetimes after introducing Mg, Ca, and Sr ions in the synthesis (Figure S5), indicating the suppression of the nonradiative recombination.

To investigate the effect of the amount of AE chlorides used on the optical and structural properties, we next chose Ca^{2+}-$CsPbCl_3$ NCs as a typical system that were synthesized by varying the feed ratio of calcium chloride ($CaCl_2$) to lead chloride ($PbCl_2$). The actual Ca concentration in NCs can be estimated by the ICP-MS. As shown in Table 1, the Ca

Table 1. Some Optical and Structural Data of Ca^{2+}-$CsPbCl_3$ NCs with Different Feed Ratios of $CaCl_2$ to $PbCl_2$

feed ratio ($CaCl_2$:$PbCl_2$)	0:1	0.5:1	1:1	2:1	3:1
Ca/Pb (mol %)	N/A	2.8	8.8	10.5	11.8
emission peak wavelength (nm)	406.5	406.3	404.9	406.1	404.8
average edge length (nm)	12.6	11.0	9.3	8.4	8.7
PLQY (%)	0.8	8.6	24.7	77.1	73.2

concentration increases with the increasing feed ratio of $CaCl_2$ to $PbCl_2$. The UV−visible absorption and PL spectra of these samples are shown in Figure 2a,b. We note that the absorption of these NCs can be slightly affected by the Ca^{2+} incorporation: the 2.8 mol % sample shows absorption band similar to that of the pristine counterpart, whereas the 8.8, 10.5, and 11.8 mol % samples demonstrate excitonic absorption bands with notably different lineshapes and slightly different absorption cutoff wavelengths (Figure 2a). This signifies that the absorbing states of NCs can be affected by the Ca^{2+} incorporation. Correspondingly, with altering the Ca^{2+} concentration, the emission peak wavelength of as-prepared samples are of tiny difference (Figure 2b, Table 1). The TEM images of pristine and 10.5 mol % Ca^{2+}-$CsPbCl_3$ NCs are shown in Figure 1b,c, and other images are shown in Figure S6a−c. The size distribution histograms of these NCs are shown in Figure S6d−f, and their average sizes are listed in Table 1. With the increase of Ca^{2+} concentration from 0 to 10.5 mol %, the average edge length of NCs decreases from 12.6 to 8.4 nm, while further increasing the concentration cannot cause a significant size variation.

The PLQY of NCs increases with the incorporation of Ca^{2+}, reaching a maximum value of 77.1% (Table 1); further increasing of the feed ratio of $CaCl_2$ to $PbCl_2$ results in a slight decrease of PLQY. Under identical measurement conditions, the PL intensity of the 10.5 mol % Ca-containing NCs is around 2 orders of magnitude stronger than that of the pristine cousin (Figure 2c). To further examine the Ca^{2+} introduction

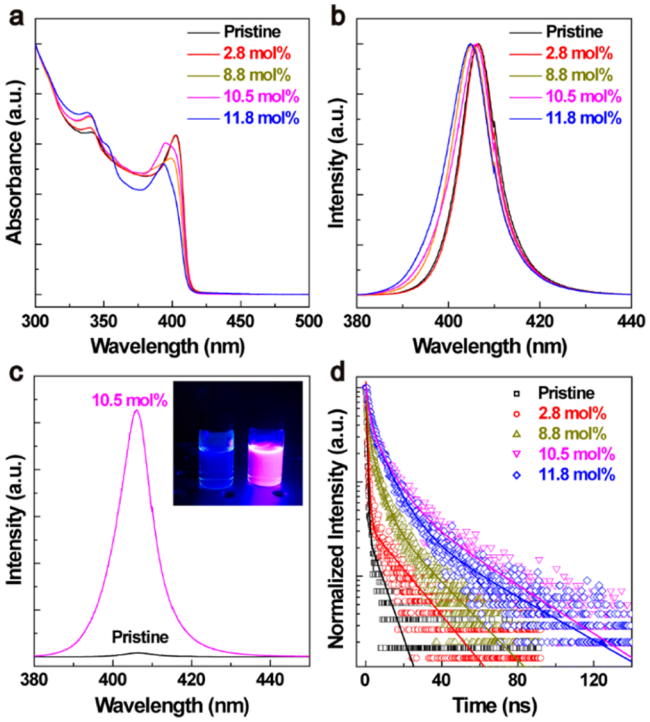

Figure 2. (a) UV−vis absorption and (b) normalized PL spectra of Ca^{2+}-$CsPbCl_3$ NCs with different Ca^{2+} concentrations. (c) PL spectra of pristine and 10.5 mol % Ca^{2+}-$CsPbCl_3$ NCs; the absorption of both NC solutions was adjusted to an optical density of 0.08. The inset shows the photographs of NC solutions under UV (365 nm) illumination, in which the left is the photograph of pristine NCs and the right is the photograph of 10.5 mol % Ca^{2+}-$CsPbCl_3$ NCs. (d) PL decay traces of Ca^{2+}-$CsPbCl_3$ NCs with different Ca^{2+} concentrations.

on the photophysical properties of NCs, we took the time-resolved PL decays (Figure 2d). All decays can be fitted well by a triexponential function, and the average lifetimes were calculated to be 2.59, 8.78, 10.30, 17.86, and 15.89 ns for 0, 2.8, 8.8, 10.5, and 11.8 mol % NCs, respectively (Table S1). Using the values of PLQY and average lifetimes, we can evaluate the radiative and nonradiative decay rates of these NCs, based on the following equations[31]

$$\Gamma_{rad} = \frac{PLQY}{\tau_{ave}} \quad (5)$$

$$\Gamma_{non\text{-}rad} = \frac{1}{\tau_{ave}} - \Gamma_{rad} = \frac{1 - PLQY}{\tau_{ave}} \quad (6)$$

where Γ_{rad} and $\Gamma_{non\text{-}rad}$ are the radiative and nonradiative recombination rates, respectively, and τ_{ave} is the average lifetime of the samples. Notably, the nonradiative recombination rate decreases from 383.01 μs^{-1} in pristine NCs to 12.82 μs^{-1} in 10.5 mol % Ca^{2+}-$CsPbCl_3$ NCs, suggesting that introducing Ca^{2+} into the $CsPbCl_3$ NCs can suppress the nonradiative recombination of $CsPbCl_3$ NCs.

To deepen the understanding of the Ca^{2+} incorporation on the photophysical properties of NCs, we further carried out the structural characterization of Ca^{2+}-$CsPbCl_3$ NCs. The X-ray photoelectron spectroscopy (XPS) was first employed to examine the change in bonding nature of our samples. The representative high-resolution XPS spectra of pristine and 10.5 mol % Ca^{2+}-$CsPbCl_3$ NCs are shown in Figure 3. The Ca 2p doublet is resolved at 347.1 and 350.9 eV, corresponding to

DOI: 10.1021/acs.chemmater.9b00442
Chem. Mater. 2019, 31, 3974−3983

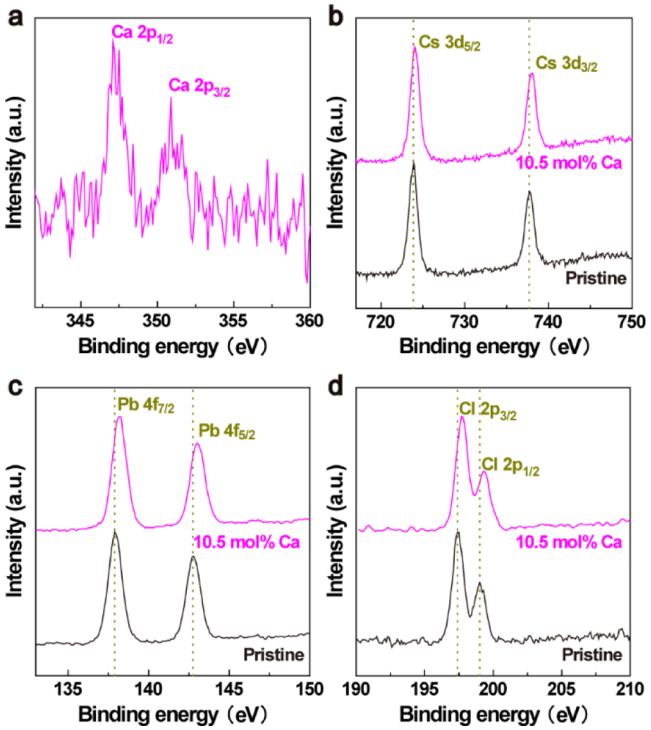

Figure 3. (a–d) High-resolution XPS spectra of Ca 2p doublet for 10.5 mol % Ca^{2+}-$CsPbCl_3$ NCs (a) and Cs 3d, (b) Pb 4f (c), and Cl 2p (d) doublet for pristine and 10.5 mol % Ca^{2+}-$CsPbCl_3$ NCs.

the binding energies of Ca $2p_{1/2}$ and Ca $2p_{3/2}$, respectively, which confirms that the valence state of Ca^{2+} is +2 (Figure 3a).[53] We further find that, compared with the pristine NCs, the binding energies of Cs $3d_{3/2}$ and Cs $3d_{5/2}$ in Ca^{2+}-$CsPbCl_3$ NCs increase by 0.1 eV, while those of Pb $4f_{5/2}$ and Pb $4f_{7/2}$ increase by 0.3 eV (Figure 3b,c). We surmise that introducing Ca^{2+} into the lattice suppresses the formation of Cl vacancies in $CsPbCl_3$ NCs, which might impact the electronic density around host cations of Cs^+ and Pb^{2+}. Interestingly, the binding energies of Cl $2p_{1/2}$ and Cl $2p_{3/2}$ also increase by 0.3 eV (Figure 3d), which is probably caused by the new bond formation of Ca–Cl. These results unambiguously evidence that the introduction of Ca^{2+} into $CsPbCl_3$ NCs can alter the chemical environment of constituent atoms.

We next conducted the X-ray absorption measurement to gain deep insights into the local coordination environment and local order around the Pb atoms. The extended X-ray absorption fine structure (EXAFS) spectra at the Pb L_{III}-edge for the 10.5 mol % Ca^{2+}-$CsPbCl_3$ NCs are shown in Figure 4a,b. In Figure 4b, we can only see one peak centered at ca. 2.3 Å (the distance not phase corrected) in *R* space, which can be attributed to the single scattering of photoelectrons by Cl atoms. The absence of other peaks in *R* space for our NCs is due to the lack of long-range structural coherence caused by the small size of NCs. We performed a single-shell fit of the EXAFS spectrum over an *R* range of 1.5–3.0 Å. We took four parameters as variables in our model: the coordination number (CN), energy shift (ΔE_0), adjustment of the half path length (ΔR), and mean-square relative displacement of Pb and Cl atoms (σ^2). All fitting results are shown in Table 2. In our previous work, we have conducted the same measurement for the pristine $CsPbCl_3$ NCs,[31] which is also shown in Table 2 for comparison. It is worth noting that the CN (5.5) in Ca^{2+}-$CsPbCl_3$ NCs is significantly larger than that in pristine NCs

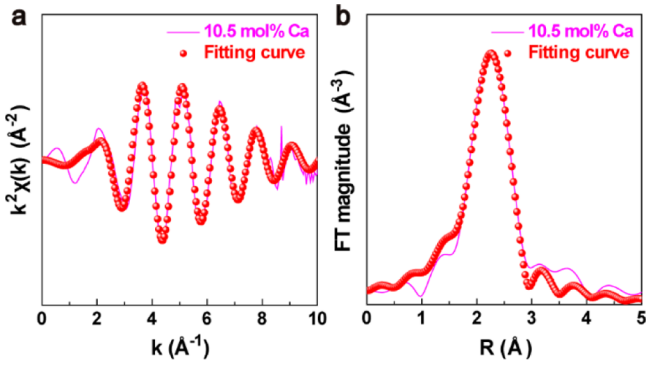

Figure 4. X-ray absorption characterization of 10.5 mol % Ca^{2+}-$CsPbCl_3$ NCs. (a) k^2-weighted Pb LIII-edge EXAFS and (b) corresponding Fourier transforms of 10.5 mol % Ca^{2+}-$CsPbCl_3$ NCs.

(3.7). This result offers a direct experimental evidence that the Ca^{2+} incorporation into the $CsPbCl_3$ NCs can suppress the formation of Cl vacancies. We point out that this inevitably affects the chemical environment of constituent atoms, as confirmed by the XPS results (Figure 3b,c). Interestingly, the σ^2 of Ca^{2+}-$CsPbCl_3$ NCs (0.014 Å^2) is slightly smaller than that of the pristine cousin (0.018 Å^2), suggesting the slightly enhanced short-range order in Ca^{2+}-$CsPbCl_3$ NCs.

Although the experimental results aforementioned suggest the elimination of trapping centers in NCs can be achieved by the Ca^{2+} incorporation, the exact distribution of Ca^{2+} ions in NCs still remains elusive. As previously reported, pyridine can be used for the removal of the surface ligand and etching of NCs.[54−56] Inspired by this, we tried to treat our samples by pyridine to intentionally destroy the surface of NCs, which makes it possible to survey the distribution of Ca^{2+} in NCs. We stress that pyridine etching did not change the crystal structure of NCs (Figure S7). After effective etching, the morphology of Ca^{2+}-$CsPbCl_3$ NCs was altered, as confirmed by the TEM image of the etched NCs (Figure 5a). Because of the lack of the surface ligand protection, the etched NCs agglomerate. However, compared with the unetched samples, the etched NCs lack the cubic morphology, suggesting effective destruction of the NC's surface. We next carried out the XPS measurement of the etched NCs. Interestingly, we cannot find notable signals assigned to Ca^{2+} (Figure 5d), which verifies that the Ca^{2+} ions were dominantly at or near the surface region of NCs. We then investigated the distribution of Sr^{2+} and Ba^{2+} ions in $CsPbCl_3$ NCs by this protocol. The TEM images also show the successful surface etching of NCs (Figure 5b,c). Similar to Ca^{2+}-$CsPbCl_3$ NCs, the etched Sr^{2+}-$CsPbCl_3$ NCs do not show any Sr^{2+} signal (Figure 5e), suggesting that the Sr^{2+} ions are also mainly at or near the surface region of NCs. However, after etching, the signal of Ba^{2+} ions is still obvious (Figure 5f).Compared with the unetched sample, the average edge length of etched Ba^{2+}-$CsPbCl_3$ NCs drops from 11.8 nm to about 4.8 nm (Figures S3c and 5c), showing complete stripping of the NC's surface. As a result, it is no doubt that Ba ions are incorporated into the core of NCs. We note that, under the same etching conditions, the etching rate for Ba^{2+}-$CsPbCl_3$ NCs is much larger than those for Ca^{2+}- and Sr^{2+}-containing cousins (Figure 5a–c), signifying the difference in their microstructures. Although not demonstrated here, we believe that the etching method reported in this work can potentially be extended to the examination of the location of

DOI: 10.1021/acs.chemmater.9b00442
Chem. Mater. 2019, 31, 3974–3983

Table 2. Main Fitting Results of the Fit Performed on the Pb LIII-Edge k^2-Weighted EXAFS Spectrum for 10.5 mol % Ca^{2+}-$CsPbCl_3$ NCs[a]

sample	shell	CN	ΔE_0 (eV)	Σ^2 ($Å_2$)	R (Å)[b]	R-factor
pristine	Pb−Cl	3.7 ± 0.8	−4.0 ± 2.1	0.018 ± 0.003	2.84 ± 0.02	0.0084
Ca^{2+}-$CsPbCl_3$ NCs	Pb−Cl	5.5 ± 1.3	−3.5 ± 2.2	0.014 ± 0.004	2.84 ± 0.02	0.0083

[a]The result of the pristine cousin is also shown for comparison.[31] [b]Distance between absorber and backscatter atoms.

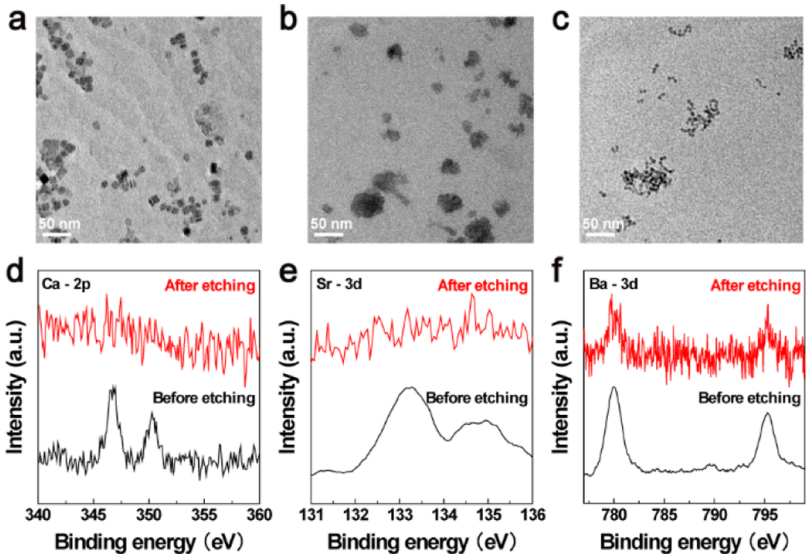

Figure 5. (a−c) TEM images of Ca^{2+}-$CsPbCl_3$ (a), Sr^{2+}-$CsPbCl_3$ (b), and Ba^{2+}-$CsPbCl_3$ (c) NCs after pyridine etching. (d−f) High-resolution XPS spectra of Ca^{2+}-$CsPbCl_3$ (d), Sr^{2+}-$CsPbCl_3$ (e), and Ba^{2+}-$CsPbCl_3$ NCs (f) with and without pyridine etching. Note that the ratio of AE^{2+} in as-synthesized Ca^{2+}, Sr^{2+}, and Ba^{2+}-$CsPbCl_3$ NCs are 10.5, 5.9,, and 12.3 mol %, respectively.

Table 3. Calculated Defect Formation Energies (in eV) in AE^{2+}-$CsPbCl_3$ NCs under Cl-Rich and Cl-Poor Conditions

	pristine		Mg-doping		Ca-doping		Sr-doping		Ba-doping	
	Cl-rich	Cl-poor	Cl-rich	Cl-poor	Cl-rich	Cl-poor	Cl-rich	Cl-poor	Cl-rich	Cl-poor
V_{Cl}	2.954	1.813	1.7777	−1.331	1.587	−1.894	1.7273	−2.136	1.8876	−2.840
V_{Cs}	1.404	2.545	0.7687	−0.058	0.526	−0.673	0.6843	−0.897	1.0936	−1.352
V_{Pb}	−2.510	1.565	3.4737	0.294	3.265	−0.287	3.4303	−0.504	3.9466	−0.852

incorporated ions in halide perovskite NCs, such as the widely studied NCs with rare earth ions.[57−60]

On the basis of the consideration of the ionic radii of AE^{2+} and Pb^{2+} ions, it is reasonable to speculate that Ca^{2+} and Sr^{2+} ions can substitute for Pb^{2+} ions that could result in the incorporation of these ions in the core, whereas Ba^{2+} ions are hard to be introduced into the core owing to a large difference in the ionic radii of Ba^{2+} and Pb^{2+} (the ionic radii of six-coordinate Ba^{2+} and Pb^{2+} ions are 1.35 and 1.19 Å, respectively,[41] Table S2). We point out that this plausible explanation has been widely used in most AE^{2+}-doped lead halide perovskites.[42−48] However, our experimental results in the context of AE^{2+}-$CsPbCl_3$ NCs suggests an adverse phenomenon: Ca^{2+} and Sr^{2+} ions can only be at/near the NC's surface, while Ba^{2+} can enter the core region of NCs. To deepen the understanding of this abnormal phenomenon, we then performed first-principles calculations (see details in the Experimental Section). Note that for all calculations, we assume that Pb^{2+} ions are replaced by AE^{2+} ions in $CsPbCl_3$. We first calculated the defect formation energies under Cl-poor and Cl-rich conditions. Interestingly, we find that the introduction of any AE^{2+} ion is detrimental for the stabilization of $CsPbCl_3$ lattice under Cl-poor conditions. As shown in Table 3, compared with pristine NCs with vacancies, it is obvious that doping of AE^{2+} ions would decrease the defect formation energies for the cases with V_{Cl} (V_{Cs}) and AE^{2+} dopants, under either Cl-rich or Cl-poor conditions. In particular, for Ba^{2+}-doped $CsPbCl_3$, the defect formation energies significantly decrease to below zero under Cl-poor conditions, suggesting ready incorporation of Ba^{2+} ions and atomic vacancies; we note that such a growth condition could occur as the reaction proceeds. This result suggests that substituting Ba^{2+} for Pb^{2+} would form a more defective lattice, which is in accordance with the above optical data of Ba^{2+}-$CsPbCl_3$ NCs. Similarly, our theoretical results also signify that the substitution of Ca^{2+} and Sr^{2+} for Pb^{2+} ions leads to ready formation of more atomic point defects such as V_{Cl} and V_{Cs}. We note that, although V_{Cs} and V_{Pb} cannot introduce deep trap states in the band gap of AE^{2+}-$CsPbCl_3$, V_{cl} can cause the formation of such traps that can effectively capture the photogenerated charge carriers (Figures S8−S11). That is, if Ca^{2+} and Sr^{2+} ions substitute for Pb^{2+} ions in the core of NCs, they should be less efficient in PL emissions. However, the experimental results show that the incorporation of Ca^{2+} or Sr^{2+} into $CsPbCl_3$ NCs can greatly boost their PLQYs, indicating that it is impossible for Ca^{2+}(Sr^{2+}) ions to substitute for Pb^{2+} ions. Combined with the EXAFS and XPS results, we conclude that Ca^{2+} or Sr^{2+} ions are merely situated at/near the

DOI: 10.1021/acs.chemmater.9b00442
Chem. Mater. 2019, 31, 3974−3983

surface of NCs, probably through an incorporation process different from Ba^{2+} ions.

We note that colloidal NCs, not limited to $CsPbX_3$ studied here, are typically grown using colloidal synthesis at lower temperatures, which corresponds to growth conditions featuring thermal nonequilibrium. As a result, the incorporation of dopants into NCs can be viewed as a kinetic process that is intimately associated with adsorption of dopant ions during the growth of NCs.[61−65] This process involves competitive adsorption of constituent atoms and dopants, and the exact growth conditions would change as the reaction proceeds. On the basis of the combined experimental and theoretical evidence, we propose the following plausible model for the explanation of the observed phenomena, as schematically illustrated in Figure 6. First, for Mg^{2+}-$CsPbCl_3$ NCs, the

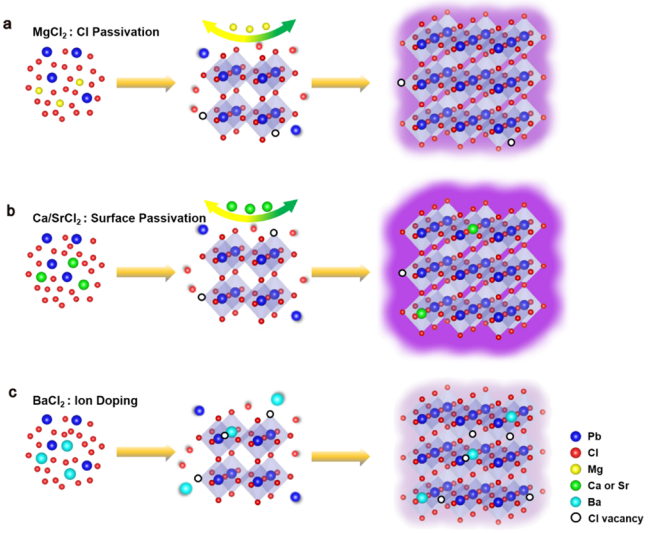

Figure 6. (a−c) Schematic illustration of the proposed passivation and doping models for Mg^{2+}-$CsPbCl_3$ NCs (a), Ca^{2+} or Sr^{2+}-$CsPbCl_3$ NCs (b) and Ba^{2+}-$CsPbCl_3$ NCs (c). Note that the Cs^+ ions are not shown to simplify the illustration.

ionic radius of Mg^{2+} is much smaller than that of Pb^{2+} (Table S2), which probably causes a notable self-purification effect of NCs that results in the exclusion of Mg^{2+} ions outside the lattice. Even in the final stage of the synthesis, Mg^{2+} ions are hard to unite with $CsPbCl_3$ NC because the bond dissociation energy of Mg−Cl is only 312 kJ mol^{-1} that is comparable to that of Pb−Cl (Table S2). As a consequence, Mg^{2+}-$CsPbCl_3$ NCs feature the absence of the Mg element. Additionally, we used $MgCl_2$ in the synthesis, which brings in excess Cl ions and create a Cl-richer synthetic condition. This is favorable for the suppression of V_{Cl} in $CsPbCl_3$ (Table 3), which may be the dominant reason for the enhanced PLQY in Mg^{2+}-$CsPbCl_3$ NCs with respect to the pristine cousin (Figure 6a). Second, for Ca^{2+}-$CsPbCl_3$ NCs (as same as Sr^{2+}-$CsPbCl_3$), at the early stage of NC formation, compared with foreign metal ions, Pb^{2+} ions preferentially involve in the growth of NCs. However, at the final stage of NC growth, the constituent atoms gradually deplete in the reaction solution, while the Ca^{2+} ions are still abundant. In such an environment, the Ca^{2+} ions can bind tightly onto the NC's surface because of the large bond dissociation energy of Ca−Cl (Table S2). We speculate that Ca^{2+} (or Sr^{2+}) isovalently occupies the Pb^{2+} crystallographic sites and results in the formation of a passivation layer at the NC's surface, as suggested by the XPS results (Figure 5). The formation of such a layer decreases the concentration of point defects caused by constituent atoms at the NC's surface (e.g., some undercoordinated Pb^{2+} ions) (Figure 6b), which results in the improved short-range order of the lattice, as evidenced by the EXAFS results (Figure 4). As for Ba^{2+}-$CsPbCl_3$ NCs, the bond dissociation energy of Ba−Cl (443 kJ mol^{-1}) is so large that the Ba^{2+} ions probably can enter the lattice of NCs even at the early stage of NC growth. Nevertheless, owing to the large ionic radius of Ba^{2+} than Pb^{2+} (1.35 Å vs 1.19 Å), doping of Ba^{2+} ions can increase the local strain of the lattice, giving rise to more chances to the formation of atomic point defects, as suggested by first-principles calculations (Table 3). The appearance of such defects may further trigger the incorporation of more Ba^{2+} ions into NCs, thus leading to the successful doping of Ba^{2+} in the core region (Figure 6c). However, these Ba^{2+}-$CsPbCl_3$ NCs contain a large number of structural defects, as reflected by the extremely low PLQY. We emphasize that the incorporation of large-sized Ba^{2+} ions into the core of NCs causes the expansion of the lattice, as evidenced by the slight low-angle shift of diffraction peaks (Figures 1a and S2).

CONCLUSIONS

In summary, we have successfully developed various AE^{2+}-$CsPbCl_3$ perovskite NCs and maximized the PLQY of these violet-emitting perovskite NCs to as high as 77.1%. Detailed experimental and theoretical characterization confirmed that Ca^{2+} and Sr^{2+} ions are present at/near the surface of NCs and form a passivation layer, but Ba^{2+} ions enter the core of NCs. The combined optical and structural characterizations show that the created passivation layer in Ca^{2+}-$CsPbCl_3$ NCs can suppress the formation of atomic vacancies, resulting in enhanced short-range order of the lattice and thus suppressing the nonradiative recombination pathways in NCs. Finally, we proposed a plausible model for the observed AE-metal-dependent passivation of $CsPbCl_3$ NCs. We emphasize that, compared with the post-synthetic surface treatment strategy, our work offers a concept of one-pot synthetic surface treatment of $CsPbCl_3$ NCs, which can be potentially extended for the synthesis of other classes of halide NCs. It is also of interest to investigate the exact local environment of Ba^{2+} ions in Ba^{2+}-$CsPbCl_3$ NCs, which will be one focus of our future work. We believe that the knowledge gained here offers a new perspective to obtain high-efficient violet-emitting perovskite NCs and will also lead to a deeper understanding of the functions that AE^{2+} ions play in the optimization of perovskite optoelectronic devices.

ASSOCIATED CONTENT

Supporting Information

The Supporting Information is available free of charge on the ACS Publications website at DOI: 10.1021/acs.chemmater.9b00442.

Detailed method for the measurement of the PLQY, additional TEM images, size distribution histograms, PL decay traces, bond structure and DOS, fitted excitonic lifetimes, radiative and nonradiative decay rates, and supplementary tables (PDF)

DOI: 10.1021/acs.chemmater.9b00442
Chem. Mater. 2019, 31, 3974−3983

AUTHOR INFORMATION

Corresponding Authors

*E-mail: zjy@buaa.edu.cn (J.Z.).
*E-mail: timothyhsun@gmail.com (H.-T.S.).

ORCID

Jia-Kai Chen: 0000-0002-4348-3132
Osman M. Bakr: 0000-0002-3428-1002
Junying Zhang: 0000-0002-4860-8774
Hong-Tao Sun: 0000-0002-0003-7941

Author Contributions

¶J.-K.C., J.-P.M., and S.-Q.G. contributed equally to this work.

Notes

The authors declare no competing financial interest.

ACKNOWLEDGMENTS

This work was supported by the National Natural Science Foundation of China (grant nos. 11874275, 11574225, and 51672106), a project funded by the Priority Academic Program Development of Jiangsu Higher Education Institutions (PAPD), and a project supported by State Key Laboratory of Luminescence and Applications. The SPring-8 experiment was carried out with the approval of the Japan Synchrotron Radiation Research Institute (JASRI; Proposal No. 2018B0074 and 2019A0068). We thank the staff at the BL14W1 beamline at the Shanghai Synchrotron Radiation Facility for XAFS measurements. First-principles calculations were performed on TianHe-1(A) at National Supercomputer Center in Tianjin.

REFERENCES

(1) Kojima, A.; Teshima, K.; Shirai, Y.; Miyasaka, T. Organometal halide perovskites as visible-light sensitizers for photovoltaic cells. *J. Am. Chem. Soc.* **2009**, *131*, 6050−6051.

(2) Lee, M. M.; Teuscher, J.; Miyasaka, T.; Murakami, T. N.; Snaith, H. J. Efficient hybrid solar cells based on meso-superstructured organometal halide perovskites. *Science* **2012**, *338*, 643−647.

(3) Heo, J. H.; Im, S. H.; Noh, J. H.; Mandal, T. N.; Lim, C.-S.; Chang, J. A.; Lee, Y. H.; Kim, H.-j.; Sarkar, A.; Nazeeruddin, M. K.; Grätzel, M.; Seok, S. I. Efficient inorganic-organic hybrid heterojunction solar cells containing perovskite compound and polymeric hole conductors. *Nat. Photonics* **2013**, *7*, 486−491.

(4) Akkerman, Q. A.; Gandini, M.; Di Stasio, F.; Rastogi, P.; Palazon, F.; Bertoni, G.; Ball, J. M.; Prato, M.; Petrozza, A.; Manna, L. Strongly emissive perovskite nanocrystal inks for high-voltage solar cells. *Nat. Energy* **2016**, *2*, 16194.

(5) Correa-Baena, J.-P.; Saliba, M.; Buonassisi, T.; Grätzel, M.; Abate, A.; Tress, W.; Hagfeldt, A. Promises and challenges of perovskite solar cells. *Science* **2017**, *358*, 739−744.

(6) Saidaminov, M. I.; Adinolfi, V.; Comin, R.; Abdelhady, A. L.; Peng, W.; Dursun, I.; Yuan, M.; Hoogland, S.; Sargent, E. H.; Bakr, O. M. Planar-integrated single-crystalline perovskite photodetectors. *Nat. Commun.* **2015**, *6*, 8724.

(7) Yakunin, S.; Sytnyk, M.; Kriegner, D.; Shrestha, S.; Richter, M.; Matt, G. J.; Azimi, H.; Brabec, C. J.; Stangl, J.; Kovalenko, M. V.; Heiss, W. Detection of X-ray photons by solution-processed lead halide perovskites. *Nat. Photonics* **2015**, *9*, 444−449.

(8) Wei, H.; Fang, Y.; Mulligan, P.; Chuirazzi, W.; Fang, H.-H.; Wang, C.; Ecker, B. R.; Gao, Y.; Loi, M. A.; Cao, L.; Huang, J. Sensitive X-ray detectors made of methylammonium lead tribromide perovskite single crystals. *Nat. Photonics* **2016**, *10*, 333−339.

(9) Tan, Z.-K.; Moghaddam, R. S.; Lai, M. L.; Docampo, P.; Higler, R.; Deschler, F.; Price, M.; Sadhanala, A.; Pazos, L. M.; Credgington, D.; Hanusch, F.; Bein, T.; Snaith, H. J.; Friend, R. H. Bright light-emitting diodes based on organometal halide perovskite. *Nat. Nanotechnol.* **2014**, *9*, 687−692.

(10) Yuan, M.; Quan, L. N.; Comin, R.; Walters, G.; Sabatini, R.; Voznyy, O.; Hoogland, S.; Zhao, Y.; Beauregard, E. M.; Kanjanaboos, P.; Lu, Z.; Kim, D. H.; Sargent, E. H. Perovskite energy funnels for efficient light-emitting diodes. *Nat. Nanotechnol.* **2016**, *11*, 872−877.

(11) Wang, N.; Cheng, L.; Ge, R.; Zhang, S.; Miao, Y.; Zou, W.; Yi, C.; Sun, Y.; Cao, Y.; Yang, R.; Wei, Y.; Guo, Q.; Ke, Y.; Yu, M.; Jin, Y.; Liu, Y.; Ding, Q.; Di, D.; Yang, L.; Xing, G.; Tian, H.; Jin, C.; Gao, F.; Friend, R. H.; Wang, J.; Huang, W. Perovskite light-emitting diodes based on solution-processed self-organized multiple quantum wells. *Nat. Photonics* **2016**, *10*, 699−704.

(12) Yantara, N.; Bruno, A.; Iqbal, A.; Jamaludin, N. F.; Soci, C.; Mhaisalkar, S.; Mathews, N. Designing Efficient Energy Funneling Kinetics in Ruddlesden-Popper Perovskites for High-Performance Light-Emitting Diodes. *Adv. Mater.* **2018**, *30*, 1800818.

(13) Akkerman, Q. A.; D'Innocenzo, V.; Accornero, S.; Scarpellini, A.; Petrozza, A.; Prato, M.; Manna, L. Tuning the optical properties of cesium lead halide perovskite nanocrystals by anion exchange reactions. *J. Am. Chem. Soc.* **2015**, *137*, 10276−10281.

(14) Nedelcu, G.; Protesescu, L.; Yakunin, S.; Bodnarchuk, M. I.; Grotevent, M. J.; Kovalenko, M. V. Fast anion-exchange in highly luminescent nanocrystals of cesium lead halide perovskites ($CsPbX_3$, X = Cl, Br, I). *Nano Lett.* **2015**, *15*, 5635−5640.

(15) Swarnkar, A.; Chulliyil, R.; Ravi, V. K.; Irfanullah, M.; Chowdhury, A.; Nag, A. Colloidal $CsPbBr_3$ perovskite nanocrystals: luminescence beyond traditional quantum dots. *Angew. Chem.* **2015**, *127*, 15644−15648.

(16) Protesescu, L.; Yakunin, S.; Bodnarchuk, M. I.; Krieg, F.; Caputo, R.; Hendon, C. H.; Yang, R. X.; Walsh, A.; Kovalenko, M. V. Nanocrystals of cesium lead halide perovskites ($CsPbX_3$, X= Cl, Br, and I): novel optoelectronic materials showing bright emission with wide color gamut. *Nano Lett.* **2015**, *15*, 3692−3696.

(17) Li, Z.; Kong, L.; Huang, S.; Li, L. Highly luminescent and ultrastable $CsPbBr_3$ perovskite quantum dots incorporated into a silica/alumina monolith. *Angew. Chem.* **2017**, *129*, 8246−8250.

(18) Liu, F.; Zhang, Y.; Ding, C.; Kobayashi, S.; Izuishi, T.; Nakazawa, N.; Toyoda, T.; Ohta, T.; Hayase, S.; Minemoto, T.; Yoshino, K.; Dai, S.; Shen, Q. Highly luminescent phase-stable $CsPbI_3$ perovskite quantum dots achieving near 100% absolute photoluminescence quantum yield. *ACS Nano* **2017**, *11*, 10373−10383.

(19) Pan, J.; Shang, Y.; Yin, J.; De Bastiani, M.; Peng, W.; Dursun, I.; Sinatra, L.; El-Zohry, A. M.; Hedhili, M. N.; Emwas, A.-H.; Mohammed, O. F.; Ning, Z.; Bakr, O. M. Bidentate ligand-passivated $CsPbI_3$ perovskite nanocrystals for stable near-unity photoluminescence quantum yield and efficient red light-emitting diodes. *J. Am. Chem. Soc.* **2018**, *140*, 562−565.

(20) Song, J.; Li, J.; Li, X.; Xu, L.; Dong, Y.; Zeng, H. Quantum dot light−emitting diodes based on inorganic perovskite cesium lead halides ($CsPbX_3$). *Adv. Mater.* **2015**, *27*, 7162−7167.

(21) Li, X.; Wu, Y.; Zhang, S.; Cai, B.; Gu, Y.; Song, J.; Zeng, H. $CsPbX_3$ quantum dots for lighting and displays: room-temperature synthesis, photoluminescence superiorities, underlying origins and white light−emitting diodes. *Adv. Funct. Mater.* **2016**, *26*, 2435−2445.

(22) Pan, J.; Quan, L. N.; Zhao, Y.; Peng, W.; Murali, B.; Sarmah, S. P.; Yuan, M.; Sinatra, L.; Alyami, N. M.; Liu, J.; Yassitepe, E.; Yang, Z.; Voznyy, O.; Comin, R.; Hedhili, M. N.; Mohammed, O. F.; Lu, Z. H.; Kim, D. H.; Sargent, E. H.; Bakr, O. M. Highly efficient perovskite−quantum−dot light−emitting diodes by surface engineering. *Adv. Mater.* **2016**, *28*, 8718−8725.

(23) Park, Y.-S.; Guo, S.; Makarov, N. S.; Klimov, V. I. Room temperature single-photon emission from individual perovskite quantum dots. *ACS Nano* **2015**, *9*, 10386−10393.

(24) Hu, F.; Zhang, H.; Sun, C.; Yin, C.; Lv, B.; Zhang, C.; Yu, W. W.; Wang, X.; Zhang, Y.; Xiao, M. Superior optical properties of perovskite nanocrystals as single photon emitters. *ACS Nano* **2015**, *9*, 12410−12416.

(25) Rainò, G.; Nedelcu, G.; Protesescu, L.; Bodnarchuk, M. I.; Kovalenko, M. V.; Mahrt, R. F.; Stoferle, T. Single cesium lead halide

DOI: 10.1021/acs.chemmater.9b00442
Chem. Mater. 2019, 31, 3974−3983

perovskite nanocrystals at low temperature: fast single photon emission, reduced blinking, and exciton fine structure. *ACS Nano* **2016**, *10*, 2485−2490.
(26) Chen, Q.; Wu, J.; Ou, X.; Huang, B.; Almutlaq, J.; Zhumekenov, A. A.; Guan, X.; Han, S.; Liang, L.; Yi, Z.; Li, J.; Xie, X.; Wang, Y.; Li, Y.; Fan, D.; Teh, D. B. L.; All, A. H.; Mohammed, O. F.; Bakr, O. M.; Wu, T.; Bettinelli, M.; Yang, H.; Huang, W.; Liu, X. All-inorganic perovskite nanocrystal scintillators. *Nature* **2018**, *561*, 88−93.
(27) Wang, Y.; Li, X.; Song, J.; Xiao, L.; Zeng, H.; Sun, H. All-inorganic colloidal perovskite quantum dots: a new class of lasing materials with favorable characteristics. *Adv. Mater.* **2015**, *27*, 7101−7108.
(28) Wang, Y.; Li, X.; Nalla, V.; Zeng, H.; Sun, H. Solution-processed low threshold vertical cavity surface emitting lasers from all−inorganic perovskite nanocrystals. *Adv. Funct. Mater.* **2017**, *27*, 1605088.
(29) Liu, H.; Wu, Z.; Shao, J.; Yao, D.; Gao, H.; Liu, Y.; Yu, W.; Zhang, H.; Yang, B. $CsPb_xMn_{1-x}Cl_3$ perovskite quantum dots with high Mn substitution ratio. *ACS Nano* **2017**, *11*, 2239−2247.
(30) Mir, W. J.; Jagadeeswararao, M.; Das, S.; Nag, A. Colloidal Mn-doped cesium lead halide perovskite nanoplatelets. *ACS Energy Lett.* **2017**, *2*, 537−543.
(31) Yong, Z.-J.; Guo, S. Q.; Ma, J. P.; Zhang, J. Y.; Li, Z. Y.; Chen, Y. M.; Zhang, B. B.; Zhou, Y.; Shu, J.; Gu, J. L.; Zheng, L. R.; Bakr, O. M.; Sun, H. T. Doping-enhanced short-range order of perovskite nanocrystals for near-unity violet luminescence quantum yield. *J. Am. Chem. Soc.* **2018**, *140*, 9942−9951.
(32) Mondal, N.; De, A.; Samanta, A. Achieving near-unity photoluminescence efficiency for blue-violet-emitting perovskite nanocrystals. *ACS Energy Lett.* **2019**, *4*, 32−39.
(33) Parobek, D.; Roman, B. J.; Dong, Y.; Jin, H.; Lee, E.; Sheldon, M.; Son, D. H. Exciton-to-dopant energy transfer in Mn-doped cesium lead halide perovskite nanocrystals. *Nano Lett.* **2016**, *16*, 7376−7380.
(34) Zhou, D.; Liu, D.; Pan, G.; Chen, X.; Li, D.; Xu, W.; Bai, X.; Song, H. Cerium and ytterbium codoped halide perovskite quantum dots: a novel and efficient downconverter for improving the performance of silicon solar cells. *Adv. Mater.* **2017**, *29*, 1704149.
(35) Das Adhikari, S.; Dutta, S. K.; Dutta, A.; Guria, A. K.; Pradhan, N. Chemically tailoring the dopant emission in manganese−doped $CsPbCl_3$ perovskite nanocrystals. *Angew. Chem., Int. Ed.* **2017**, *129*, 8872−8876.
(36) Zhou, Y.; Chen, J.; Bakr, O. M.; Sun, H. T. Metal-doped lead halide perovskites: synthesis, properties, and optoelectronic applications. *Chem. Mater.* **2018**, *30*, 6589−6613.
(37) Ahmed, T.; Seth, S.; Samanta, A. Boosting the photoluminescence of $CsPbX_3$ (X= Cl, Br, I) perovskite nanocrystals covering a wide wavelength range by post-synthetic treatment with tetrafluoroborate salts. *Chem. Mater.* **2018**, *30*, 3633−3637.
(38) Ahmed, G. H.; El-Demellawi, J. K.; Yin, J.; Pan, J.; Velusamy, D. B.; Hedhili, M. N.; Alarousu, E.; Bakr, O. M.; Alshareef, H. N.; Mohammed, O. F. Giant photoluminescence enhancement in $CsPbCl_3$ perovskite nanocrystals by simultaneous dual-surface passivation. *ACS Energy Lett.* **2018**, *3*, 2301−2307.
(39) Li, F.; Liu, Y.; Wang, H.; Zhan, Q.; Liu, Q.; Xia, Z. Postsynthetic surface trap removal of $CsPbX_3$ (X= Cl, Br, or I) quantum dots via a ZnX_2/hexane solution toward an enhanced luminescence quantum yield. *Chem. Mater.* **2018**, *30*, 8546−8554.
(40) Behera, R. K.; Das Adhikari, S.; Dutta, S. K.; Dutta, A.; Pradhan, N. Blue-emitting $CsPbCl_3$ nanocrystals: impact of surface passivation for unprecedented enhancement and loss of optical emission. *J. Phys. Chem. Lett.* **2018**, *9*, 6884−6891.
(41) Shannon, R. D. Revised effective ionic-radii and systematic studies of interatomic distances in halides and chalcogenides. *Acta Crystallogr., Sect. A: Cryst. Phys., Diffr., Theor. Gen. Crystallogr.* **1976**, *32*, 751−767.
(42) Navas, J.; Sánchez-Coronilla, A.; Gallardo, J. J.; Hernández, N. C.; Piñero, J. C.; Alcántara, R.; Fernández-Lorenzo, C.; Desireé, M.; Aguilar, T.; Martín-Calleja, J. New insights into organic−inorganic hybrid perovskite $CH_3NH_3PbI_3$ nanoparticles. An experimental and theoretical study of doping in Pb^{2+} sites with Sn^{2+}, Sr^{2+}, Cd^{2+} and Ca^{2+}. *Nanoscale* **2015**, *7*, 6216−6229.
(43) Pérez-del-Rey, D.; Forgács, D.; Hutter, E. M.; Savenije, T. J.; Nordlund, D.; Schulz, P.; Berry, J. J.; Sessolo, M.; Bolink, H. J. Strontium insertion in methylammonium lead iodide: long charge carrier lifetime and high fill−factor solar cells. *Adv. Mater.* **2016**, *28*, 9839−9845.
(44) Shai, X.; Zuo, L.; Sun, P.; Liao, P.; Huang, W.; Yao, E.-P.; Li, H.; Liu, S.; Shen, Y.; Yang, Y.; Wang, M. Efficient planar perovskite solar cells using halide Sr-substituted Pb perovskite. *Nano Energy* **2017**, *36*, 213−222.
(45) Chan, S.-H.; Wu, M. C.; Lee, K. M.; Chen, W. C.; Lin, T. H.; Su, W. F. Enhancing perovskite solar cell performance and stability by doping barium in methylammonium lead halide. *J. Mater. Chem. A* **2017**, *5*, 18044−18052.
(46) Lau, C. F. J.; Deng, X.; Zheng, J.; Kim, J.; Zhang, Z.; Zhang, M.; Bing, J.; Wilkinson, B.; Hu, L.; Patterson, R.; Huang, S.; Ho-Baillie, A. Enhanced performance via partial lead replacement with calcium for a $CsPbI_3$ perovskite solar cell exceeding 13% power conversion efficiency. *J. Mater. Chem. A* **2018**, *6*, 5580−5586.
(47) Lu, M.; Zhang, X.; Zhang, Y.; Guo, J.; Shen, X.; Yu, W. W.; Rogach, A. L. Simultaneous strontium doping and chlorine surface passivation improve luminescence intensity and stability of $CsPbI_3$ nanocrystals enabling efficient light−emitting devices. *Adv. Mater.* **2018**, *30*, 1804691.
(48) Yao, J.-S.; Ge, J.; Wang, K.-H.; Zhang, G.; Zhu, B.-S.; Chen, C.; Zhang, Q.; Luo, Y.; Yu, S.-H.; Yao, H.-B. Few-nanometer-sized α-$CsPbI_3$ quantum dots enabled by strontium substitution and iodide passivation for efficient red light emitting diodes. *J. Am. Chem. Soc.* **2019**, *141*, 2069−2079.
(49) Kresse, G.; Furthmüller, J. Efficient iterative schemes for ab initio total-energy calculations using a plane-wave basis set. *Phys. Rev. B* **1996**, *54*, 11169−11186.
(50) Kresse, G.; Joubert, D. From Ultrasoft Pseudopotentials to the Projector Augmented-Wave Method. *Phys. Rev. B* **1999**, *59*, 1758−1775.
(51) Perdew, J. P.; Burke, K.; Ernzerhof, M. Generalized gradient approximation made simple. *Phys. Rev. Lett.* **1996**, *77*, 3865−3868.
(52) Zhang, J.; Dang, W.; Ao, Z.; Cushing, S. K.; Wu, N. Band gap narrowing in nitrogen-doped $La_2Ti_2O_7$ predicted by density-functional theory calculations. *Phys. Chem. Chem. Phys.* **2015**, *17*, 8994−9000.
(53) Baer, D. R.; Blanchard, D. L.; Engelhard, M. H.; Zachara, J. M. The interaction of water and Mn with surfaces of $CaCO_3$: an XPS study. *Surf. Interface Anal.* **1991**, *17*, 25−30.
(54) Mikulec, F. V.; Kuno, M.; Bennati, M.; Hall, D. A.; Griffin, R. G.; Bawendi, M. G. Organometallic synthesis and spectroscopic characterization of manganese-doped CdSe nanocrystals. *J. Am. Chem. Soc.* **2000**, *122*, 2532−2540.
(55) Hanif, K. M.; Meulenberg, R. W.; Strouse, G. F. Magnetic ordering in doped $Cd_{1-x}Co_xSe$ diluted magnetic quantum dots. *J. Am. Chem. Soc.* **2002**, *124*, 11495−11502.
(56) Kuno, M.; Lee, J. K.; Dabbousi, B. O.; Mikulec, F. V.; Bawendi, M. G. The band edge luminescence of surface modified CdSe nanocrystallites: probing the luminescing state. *J. Chem. Phys.* **1997**, *106*, 9869−9882.
(57) Pan, G.; Bai, X.; Yang, D.; Chen, X.; Jing, P.; Qu, S.; Zhang, L.; Zhou, D.; Zhu, J.; Xu, W.; Dong, B.; Song, H. Doping lanthanide into perovskite nanocrystals: highly improved and expanded optical properties. *Nano Lett.* **2017**, *17*, 8005−8011.
(58) Milstein, T. J.; Kroupa, D. M.; Gamelin, D. R. Picosecond quantum cutting generates photoluminescence quantum yields over 100% in ytterbium-doped $CsPbCl_3$ nanocrystals. *Nano Lett.* **2018**, *18*, 3792−3799.
(59) Zhang, X.; Zhang, Y.; Zhang, X.; Yin, W.; Wang, Y.; Wang, H.; Lu, M.; Li, Z.; Gu, Z.; Yu, W. W. Yb^{3+} and Yb^{3+}/Er^{3+} doping for near-

DOI: 10.1021/acs.chemmater.9b00442
Chem. Mater. 2019, 31, 3974−3983

infrared emission and improved stability of $CsPbCl_3$ nanocrystals. *J. Mater. Chem. C* **2018**, *6*, 10101−10105.
(60) Ma, J. P.; Chen, Y. M.; Zhang, L. M.; Guo, S. Q.; Liu, J. D.; Li, H.; Ye, B. J.; Li, Z. Y.; Zhou, Y.; Zhang, B. B.; Bakr, O. M.; Zhang, J. Y.; Sun, H. T. Insights into the local structure of dopants, doping efficiency, and luminescence properties of lanthanide-doped $CsPbCl_3$ perovskite nanocrystals. *J. Mater. Chem. C* **2019**, *7*, 3037.
(61) Radovanovic, P. V.; Norberg, N. S.; McNally, K. E.; Gamelin, D. R. Colloidal transition-metal-doped ZnO quantum dots. *J. Am. Chem. Soc.* **2002**, *124*, 15192−15193.
(62) Erwin, S. C.; Zu, L.; Haftel, M. I.; Efros, A. L.; Kennedy, T. A.; Norris, D. J. Doping semiconductor nanocrystals. *Nature* **2005**, *436*, 91−94.
(63) Du, M.-H.; Erwin, S. C.; Efros, A. L. Trapped-dopant model of doping in semiconductor nanocrystals. *Nano Lett.* **2008**, *8*, 2878−2882.
(64) Singh, T.; Mountziaris, T. J.; Maroudas, D. On the transition-metal doping efficiency of zinc oxide nanocrystals. *Appl. Phys. Lett.* **2010**, *97*, 073120.
(65) Jansons, A. W.; Koskela, K. M.; Crockett, B. M.; Hutchison, J. E. Transition metal-doped metal oxide nanocrystals: efficient substitutional doping through a continuous growth process. *Chem. Mater.* **2017**, *29*, 8167−8176.

DOI: 10.1021/acs.chemmater.9b00442
Chem. Mater. 2019, 31, 3974−3983